ACS OMEGA

Article

Cite This: ACS Omega 2019, 4, 21410−21416

http://pubs.acs.org/journal/acsodf

Cerium Hexacyanocobaltate: A Lanthanide-Compliant Prussian Blue Analogue for Li-Ion Storage

Kaiqiang Zhang,[†,§] Tae Hyung Lee,[†] Joo Hwan Cha,[‡] Rajender S. Varma,[*,∥] Ji-Won Choi,[*,§] Ho Won Jang,[*,†] and Mohammadreza Shokouhimehr[*,†]

[†]Department of Materials Science and Engineering, Research Institute of Advanced Materials, Seoul National University, Seoul 08826, Republic of Korea

[‡]Small and Medium Enterprises Support Center, Korea Institute of Science and Technology (KIST), Seoul 02792, Republic of Korea

[§]Electronic Materials Center, Korea Institute of Science and Technology (KIST), Seoul 136-791, Republic of Korea

[∥]Regional Centre of Advanced Technologies and Materials, Faculty of Science, Palacky University in Olomouc, Šlechtitelů 27, 783 71 Olomouc, Czech Republic

Supporting Information

ABSTRACT: Electrode materials are the most significant components of lithium-ion batteries (LIBs) and play an important role in endowing them with high electrochemical performance. The exploration of new electrode materials and their comparative study with contemporary resources will help the design of advanced electrodes. Here, we have synthesized a new type of Prussian blue analogue (cerium(III) hexacyanocobaltate, CeHCCo) and systematically explored the effect of valence states of Fe^{2+} and Ce^{3+} on crystal structure and electrochemical properties of final products. We demonstrate that the unbalanced charge in iron(II) hexacyanocobaltate (FeHCCo), as opposed to that in CeHCCo, results in more residual K^+ ions, thereby leading to the occupancy of cavities. As a result, the K^+ ion-rich FeHCCo exhibits lower capacities of 55 ± 3 and 15 ± 3 mAh g^{-1} at 0.1 and 1 A g^{-1}, respectively, compared with the K^+ ion-deficient CeHCCo that exhibits capacities of 242 ± 3 and 111 ± 3 mAh g^{-1} at the same current densities. This work provides a novel contribution for the exploration of new Prussian blue analogues and bestows a newer concept for electrode material design.

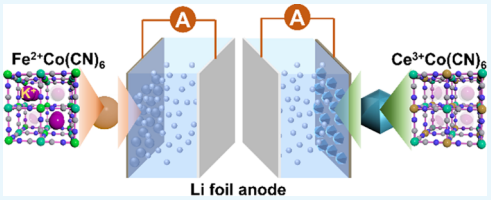

1. INTRODUCTION

Rechargeable lithium-ion batteries (LIBs) have dominated the energy storage and conversion sector for decades.[1−4] Other ion batteries such as Na^+,[5−8] K^+,[9−12] and Zn^{2+}[13,14] are being considered as alternatives to LIBs, primarily because of the high cost of lithium resources. However, we have a long way to go before we can commercialize the other alternatives. In addition, the small size and lower charge density of Li^+ ions and high energy densities of LIBs make them a promising candidate, in theory, for energy storage devices. The study of electrode materials has largely contributed to the progress of LIBs. Typically, the cost-effective Prussian blue analogues as the electrode material have exhibited high potential for the fabrication of high-performance LIBs that are used in large-scale energy conversion and storage systems.[15−18]

Prussian blue analogues were synthesized as metal−organic frameworks wherein the transition metal ions were alternately bridged to the ends of cyanide linkers. They have served as functional materials in various fields such as gas absorption,[19,20] drug delivery,[21,22] ion conductors,[23−25] and catalysts.[26,27] The numerous advantages such as an intrinsic robust crystal structure, facile preparation process, reasonable capacity, and low cost make the Prussian blue analogues suitable for use as electrode materials in LIBs.[28−30] The general formula of Prussian blue analogues is $A_yP[R(CN)_6]_{1-x}\square_x \cdot nH_2O$ where A is an alkali metal mobile cation, P is the nitrogen-coordinated transition metal ion, R is the carbon-coordinated transition-metal ion, and □ is $[R(CN)_6]^{n-}$ ion vacancies ($0 \le y \le 2$ and $0 \le x \le 1$). In the crystal framework, eight subunits are constructed in each unit for the Li^+ ion intercalation and deintercalation during the discharging and charging processes, respectively. This unique structure plays a significant role in the electrochemical reaction.[31] Thus, it is imperative to study the structure of Prussian blue analogues for their performance as electrode materials in LIBs.

Considering that the valence state of the final structure is dependent on the valence state of the precursor, we report here the effect of valence states of the initial reactants on the electrochemical properties of the cathode materials in LIBs. To obtain a trivalent metal ion, which is stable in aqueous solutions to match with the hexacyanocobaltate, we synthesized cerium(III) hexacyanocobaltate (CeHCCo). Furthermore, comprehensive characterization and analysis revealed that the residual K^+ ion content in iron(II) hexacyanocobaltate

Received: September 21, 2019
Accepted: November 15, 2019
Published: December 2, 2019

DOI: 10.1021/acsomega.9b03104
ACS Omega 2019, 4, 21410−21416

(FeHCCo) was greater than that in CeHCCo, resulting in a significant decay in the capacity. In addition, these two electrode materials exhibit a surface-controlled Li-ion storage nature. This work is expected to provide more insights for exploring not only a new type of Prussian blue analogues but also the design of electrode materials for advanced LIBs.

2. RESULTS AND DISCUSSION

The synthesis process and theoretical structures of FeHCCo and CeHCCo are shown in Figure 1, which illustrates that

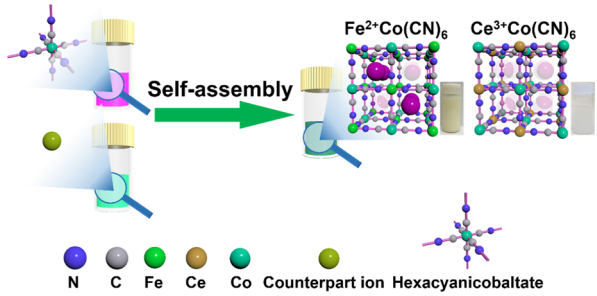

Figure 1. Synthesis process and general structural units of FeHCCo and CeHCCo. Eight subunits are present in each unit for Li^+ intercalation. Insets show the optical images of the synthesized FeHCCo and CeHCCo nanoparticles (NPs) in aqueous solutions.

there are eight subunits where Li^+ ions can anchor. Fe^{2+}/Ce^{3+} ions are coordinated to nitrogen atoms of the cyanide linkers for FeHCCo/CeHCCo. In the products, the charge neutrality requirement normally results in some inherent vacancies of $[Co(CN)_6]^{3-}$ clusters.[32] This structural difference is directly manifested in the optical color (Figure 1, glass vials, insets) due to the different optical properties of the metal−cyanide−metal coordination.

The morphology is studied by scanning electron microscopy (SEM) and transmission electron microscopy (TEM). A distinct difference in the morphologies of FeHCCo and CeHCCo (Figure 2a,d) can be observed. FeHCCo exhibits

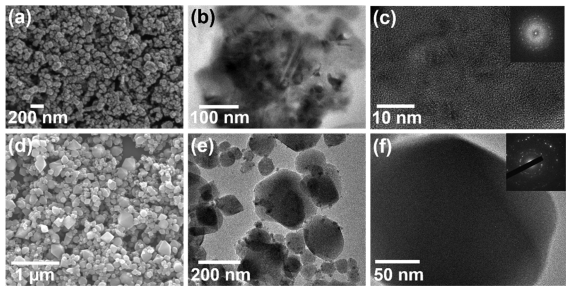

Figure 2. (a) SEM, (b) TEM, and (c) HRTEM images of the synthesized FeHCCo NPs and corresponding selected area electron diffraction patterns. (d) SEM, (e) TEM, and (f) HRTEM images of the synthesized CeHCCo NPs and corresponding selected area electron diffraction patterns.

spherical NPs with a size of ∼20 nm, while polyhedron-shaped CeHCCo NPs are formed with multiple sizes; the smaller FeHCCo NPs have a smooth surface, which is further illustrated in the TEM images (Figure 2b). Correspondingly, the CeHCCo NPs have a size larger than that of FeHCCo NPs, also displayed in a TEM image (Figure 2e). The crystalline particles and diffraction patterns (Figure 2c,f) demonstrate the polycrystalline feature. Furthermore, the atomic arrangement can be observed in the high-resolution TEM (HRTEM) images with an interplanar spacing of approximately 0.44 nm for FeHCCo and 0.41 nm for CeHCCo (Figure S1).

Both FeHCCo and CeHCCo NPs exhibit crystallized features, suggesting that manifestation is independent of the initial reactants. However, the large variation in the particle size and morphology implies that the crystal growth is greatly dependent on the initial reactants, which is consistent with other reports.[33] The consistent elements are uniformly distributed throughout the NPs (Figure S2), which is in accordance with the qualitatively verified results by the energy-dispersive X-ray (EDX) mapping (Figures S2b,d and S3).

The crystal structure of FeHCCo determined by X-ray diffraction (XRD, Figure 3a) are well indexed into a cubic

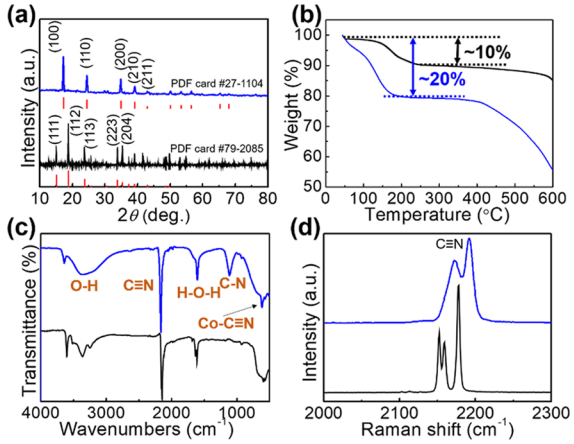

Figure 3. (a) XRD, (b) TGA, (c) FT-IR, and (d) Raman spectra of the synthesized FeHCCo (blue) and CeHCCo (black) products.

structure ($a = b = c = 5.2$ Å). However, CeHCCo shows an orthorhombic crystal structure with enhanced lattice constants ($a = 7.4$, $b = 12.9$, and $c = 13.7$ Å) by referring to $ErFe(CN)_6$ (PDF card: #79-2085, Cmcm(63)), which is expected to facilitate the Li^+ ions' transfer inside the material. The characteristic peaks of both products are well indexed in Figure 3a. A similar occurrence is where crystallization, regardless of the initial reactants, is confirmed by the representative characteristic diffraction peaks in the XRD spectra of both FeHCCo and CeHCCo. The well-constructed frameworks are critical for the Li^+ ion intercalation/deintercalation during the charge and discharge processes.

The thermal stability of the synthesized FeHCCo and CeHCCo is examined using thermal gravimetric analysis (TGA, Figure 3b) by varying the temperature from room temperature to 600 °C. The initial weight loss corresponds to the release of zeolitic and coordinated water species.[34] A sharp decrease in the weights after 450 °C indicates poor thermal stability for FeHCCo compared with CeHCCo with a platform until 600 °C, demonstrating more bond energy for CeHCCo than that for FeHCCo. The loss of water (∼20% by weight) for FeHCCo is two times more than that of CeHCCo, which is more likely due to the fully bonded $[Co(CN)_6]^{3-}$ by Ce^{3+} resulting in less coordinated water.[35−37]

The molecular formulas based on Fe/Ce are deduced (based on X-ray fluorescence (XRF) results in Table S1) to be $K_{0.6}Fe[Co(CN)_6]_{0.72}\square_{0.28}$ and $K_{0.01}Ce[Co(CN)_6]_{0.99}\square_{0.01}$.

DOI: 10.1021/acsomega.9b03104
ACS Omega 2019, 4, 21410−21416

The related qualitative analysis of the constituent elements displayed in Figure S4 agrees well with the EDX results (Figures S2 and S3). A larger amount of the K^+ impurity, trapped at the subunits to balance the valence state, suggested more cyanide vacancies in the FeHCCo NPs (0.28) than those (0.01) of CeHCCo. The elemental amounts are further confirmed by inductively coupled plasma (ICP, Table S2). As a sequence, the composition of K in the FeHCCo is much higher than that in CeHCCo, which agrees with the XRF results.

To confirm the cyanide-constructed crystal structure, the representative cyanide stretching bands in the Fourier transform infrared spectroscopy (FT-IR) spectra are detected at around 2200 and 500 cm^{-1} (Figure 3c). The H−O−H stretching band at around 1600 cm^{-1} and O−H stretching band at around 3400 cm^{-1} further verify the presence of the residual water molecules and their coordination. The C−N band at around 1210 cm^{-1} in FeHCCo may be due to the coordination from atmospheric nitrogen.[38]

The Raman spectra (Figure 3d) of the products are obtained from 2000 to 2300 cm^{-1} to confirm the valence state of cyanide-bonded metal ions as they are sensitive to the oxidation states of the metal ions.[39,40] The obvious bands at 2171 and 2192 cm^{-1} for FeHCCo and 2163 and 2182 cm^{-1} for CeHCCo are assigned to the stretching mode of the cyanide bridges. A small Raman shift in the stretching mode of the cyanide bridge is exhibited when the oxidation state of Fe^{2+} changes to Ce^{3+}, which results in a higher energy of the stretching band.[41]

The surface chemical compositions and coordination of the prepared FeHCCo and CeHCCo are measured by X-ray photoelectron spectroscopy (XPS, Figure 4 and Figure S5). In the wide survey spectrum (Figure S5), the O 1s peak in FeHCCo exhibits a higher intensity than that in CeHCCo directly demonstrating more coordinated water molecules due to the $[Co(CN)_6]^{3-}$ vacancies as per the molecular formulas we deduced. There is no obvious difference in the deconvoluted spectra of C 1s and N 1s (Figure S5) where the cyanide functional group within the frameworks is distinctly detected. Two pairs of doublet peaks are exhibited in deconvoluted Ce 3d at binding energies of approximately 885 and 905 eV. The binding energy at 883 eV confirms the existing Ce^{3+} ions inside the frameworks (Figure 4d). The Fe^{3+} in FeHCCo is more likely due to the electron transfer from Fe^{2+} to Co^{3+} through the cyanide bridge.[42−46] This electron transfer behavior can be further confirmed by the difference in binding energy of deconvoluted N 1s (Figure S5d,f), together with the formed Co^{2+}. Similarly, the Ce^{4+} ions in the deconvoluted Ce 3d also suggest the underlying charge transfer.

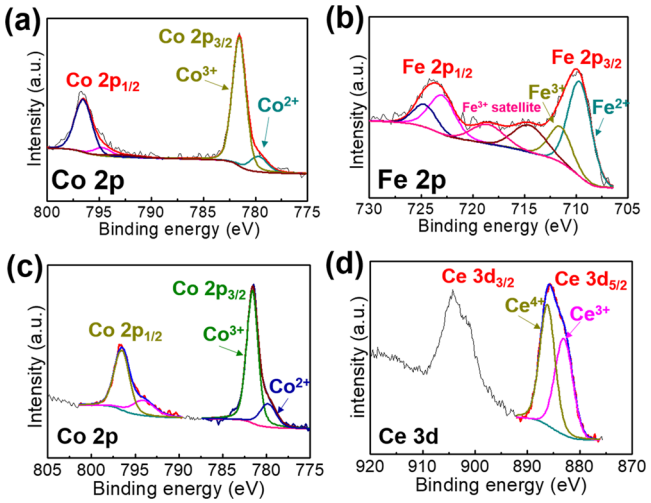

Figure 4. Deconvoluted XPS spectra of (a) Co 2p and (b) Fe 2p for FeHCCo and (c) Co 2p and (d) Ce 3d for CeHCCo.

Based on the above analysis, a feasible growth mechanism for CeHCCo NPs can be obtained. Ce^{3+}, $[Co(CN)_6]^{3-}$, and K^+ are the primary existing species in the initial solution. To lower the total energy raised by the opposite charges, the crystal growth proceeds in a directional manner for CeHCCo. The high-valence Ce−N is expected to be more stable because of its higher crystal field stabilization energy.[47,48] With increasing time, CeHCCo with six-fold-coordinated Ce^{3+} possesses a promising and robust structural stability, and its growth proceeds toward the polyhedral crystal morphology. The directional growth can be achieved by taking advantage of the oriented assembly enabled by the high selectivity of facet bonding as pursued by a previous report.[49] Due to the fixed vector angles of every two facets within one family such as 90° or 180° for {100} facets, etc., we thus infer that the CeHCCo product directionally grows along the <110> crystallographic orientation with a 60° vector angle. Furthermore, a similar crystal structural morphology was found in a previous report by Lin et al., which was formed via a controllable epitaxial growth by tuning the F^- ion additive concentration in the reaction system.[50] After a comprehensive analysis, we infer that our CeHCCo product directionally grows along the <110> crystallographic orientation and is enclosed with 12 side facets; thus, the hexagonal structure was finally formed.

The effect of vacancies in the FeHCCo and CeHCCo nanocrystals on their electrochemical properties is determined by assembling these NPs as the active materials of the cathode in half cells. A redox reaction is exhibited by a pair of peaks at around 3.3 V versus Li^+/Li (cathodic) and 3.6 V versus Li^+/Li (anodic) in the cyclic voltammetry (CV) curves (Figure 5a,b) of both FeHCCo and CeHCCo. To ensure that the capacity is mainly contributed by the active materials in the subsequent measurement, a cycling test for the naked graphite current

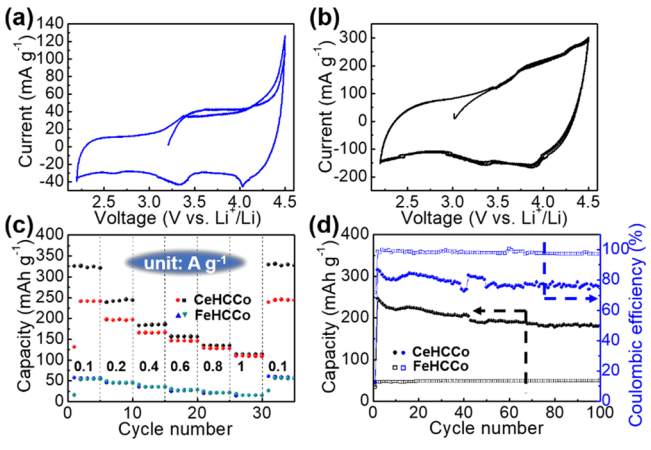

Figure 5. CV curves of (a) FeHCCo and (b) CeHCCo in the voltage range of 2.2−4.5 V vs Li^+/Li with a scan rate of 0.5 mV s^{-1}. (c) Rate performances at current densities of 0.1, 0.2, 0.4, 0.6, 0.8, and 1 A g^{-1} and (d) cycling measurements (discharge capacity) at a current density of 0.1 A g^{-1} for FeHCCo and CeHCCo.

DOI: 10.1021/acsomega.9b03104
ACS Omega 2019, 4, 21410−21416

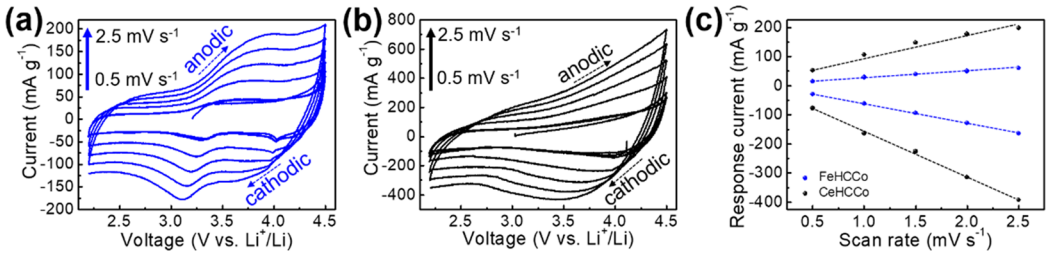

Figure 6. CV curves of (a) FeHCCo and (b) CeHCCo at various scan rates. (c) Current responses of the FeHCCo and CeHCCo at various scan rates.

collector is performed. The result shows a negligible capacity value (Figure S6c,d). The distinct increases in capacity from 55 ± 3 to 242 ± 3 mAh g^{-1} at 0.1 A g^{-1} and 15 ± 3 to 111 ± 3 mAh g^{-1} at 1 A g^{-1} are achieved when the initial reactant Fe^{2+} ion is changed into a Ce^{3+} ion (Figure 5c). Furthermore, an enhanced capacity retention for CeHCCo (46%) is achieved compared with that of FeHCCo (27%) with increasing current density from 0.1 to 1 A g^{-1}. The charge/discharge cycling stability displays the improved capacity for CeHCCo compared with that of FeHCCo (Figure 5d). Furthermore, the high performance of CeHCCo can also be demonstrated by comparing with other reported Prussian blue analogues as shown in Table S3 where a comprehensive improvement in both capacity and life span can be attained at a higher current density. Typically, higher capacities are exhibited for CeHCCo than those for both $CeHCFe^{II}$ with the same cation and $Mn_3[Co(CN)_6]_2$ with the same anion. This implies that the improved electrochemical capacities are mainly attributed to this combination. In addition, one may ask the case of Fe^{III}HCCo. For which, Fe^{III}HCCo also donates highly improved capacities compared with Fe^{II}HCCo as shown in Table S3. This agrees that the well-matched valence states are favorable for Li^+ ion storage. Furthermore, the residual K species in $K^{III}_{0.07}Fe[Co(CN)_6]_{0.89}$ is also much less than that in $K^{II}_{0.6}Fe[Co(CN)_6]_{0.72}$. This further confirms that the valence state exhibits a crucial impact on the final K^+ storage amount.[18] The significant decrease in capacity when Fe^{2+} is employed can be attributed to the greater number of residual K^+ ions trapped in Li^+ ion sites in FeHCCo, which is almost 60 times more than that in CeHCCo (Figure S7). Therefore, the Li^+ diffusion impedance is expected to be depressed. To affirm this, we conducted the electrochemical impedance spectroscopy (EIS) measurement where the decreased impedance for both FeHCCo and CeHCCo after the first five charge/discharge cycles reflects the infiltration of the electrolyte into the fresh electrode (Figure S8a,b). One key point is that the CeHCCo electrode exhibits an ∼500 ohm impedance that is much lower than ∼900 ohm of FeHCCo (Figure S8c). The EIS curve is studied under the assistance of the corresponding equivalent circuit, which comprises the internal resistance (R_s) including electrode, electrolyte, electrode/current collector contact, and current collector resistances. Furthermore, the Warburg impedance (Z_w), charge transfer resistance (R_{ct}), and double-layer capacitance (C_1) are also depicted in the provided EIS curve (Figure S8d).

To determine the stability of crystal structures, we perform XRD measurements for both FeHCCo (Figure S9a) and CeHCCo (Figure S9b) using the cathodes cast with active materials and disassembled from the half-cells after cycling tests. The distinct carbon peaks are derived from the graphite paper supports. The characteristic peaks are well preserved in the FeHCCo active material after encountering cycling tests, although decreased peak intensities are exhibited. However, different XRD diffraction patterns are obtained for CeHCCo implying the phase change during the Li ion insertion and extraction.

To further confirm the final capacity of FeHCCo and CeHCCo, CV curves are scanned at various rates (Figure 6a,b). Well-preserved CV curves are exhibited for both FeHCCo and CeHCCo without obvious distortions. An obvious hysteresis for FeHCCo when scanned at higher rates is clearly shown by the negative shift of cathodic peaks and positive shift of anodic peaks. In other words, the hysteresis in FeHCCo can reduce the capacity and stability of electrochemical reactions.[51−59] An evaluation of the capacity contribution is analyzed by the relationship between response currents and scan rates at a fixed voltage (3.1 V vs Li^+/Li) in CV curves (Figure 6c). The quasi-linear relationship for both FeHCCo and CeHCCo demonstrates the surface-control-dominated Li-ion storage mechanism. Furthermore, the higher response current for CeHCCo demonstrates the lower impedance as measured in the EIS spectra (Figure S8a−c) assisting to increase the capacity.

3. CONCLUSIONS

In summary, we have synthesized CeHCCo and studied the effect of cation nodes with different valence states on the structural and Li-ion storage electrochemical properties of both FeHCCo and CeHCCo. Both spherical FeHCCo and polyhedral CeHCCo exhibit a polycrystalline nature. The reduced K^+ impurity and impedance result in the capacity increase from 55 ± 3 to 242 ± 3 mAh g^{-1} at 0.1 A g^{-1} and 15 ± 3 to 111 ± 3 mAh g^{-1} at 1 A g^{-1}. This work presents more detailed insights in terms of exploration of new Prussian blue analogues and reactant selection for electrode material fabrication, which undeniably pave the way for the development of advanced Li-ion storage devices.

4. EXPERIMENTAL SECTION

4.1. Preparation of FeHCCo and CeHCCo. FeHCCo NPs were synthesized by a coprecipitation method by simultaneous dropwise addition of 100 mL of $FeCl_2$ (0.03 M) (Sigma-Aldrich) and 100 mL of $K_3[Co(CN)_6]$ (0.03 M, Sigma-Aldrich) to 100 mL of H_2O under constant stirring; a milky white precipitate ensued immediately. After sonicating for 30 min, the suspension was allowed to sit for 1 h. The precipitate was separated and rinsed several times with a large amount of deionized water and ethanol. It was then dried in an oven at 60 °C for further use. The synthesis of CeHCCo was carried out in a similar manner, except that cerium(III) nitrate hexahydrate (Samchun, 0.03 M) was used as the initial

DOI: 10.1021/acsomega.9b03104
ACS Omega 2019, 4, 21410−21416

reactant and the codeposition process was performed at 80 °C. During the synthesis of CeHCCo, a transparent solution, without any deposition, was obtained at room temperature, which suggested the requirement of heating treatment. In the deliberation for the appropriate heating temperature, the maximum value attainable for aqueous solutions is 100 °C. However, a transparent solution obtained at 60 °C indicates that a higher temperature is warranted. We thus synthesized CeHCCo at 80 °C, and a white deposition was obtained.

4.2. Physical Characterization. Structural study was performed using XRD (D8-Advance) equipped with Cu Kα radiation at a fixed incident angle of 2°, XPS (PHI 5000 VersaProbe) using an Al Kα source (Sigma probe, VG Scientifics), Raman spectroscopy (inVia Raman microscope), and FT-IR (Nicolet iS50) spectroscopy. The morphology and constitution were studied using FE-SEM (SUPRA 55VP), TEM (Tecnai F20), and EDX. The constitutions of the prepared FeHCCo and CeHCCo were studied by XRF (ZSX-PRIMUS) and TGA, which was carried out under a N_2 flow from room temperature to 600 °C at a heating rate of 10 °C min^{-1}. ICP spectroscopy was performed for confirming the elemental amounts of the products. Each product (0.1 g) was dissolved into 35 mL of NaOH solution for ICP measurements.

4.3. Electrode Preparation. Briefly, a slurry containing FeHCCo or CeHCCo NPs, carbon black (Super P Li), and poly(vinylidene)difluoride in a mass ratio of 7:2:1 was prepared by manually grinding the materials and dispersing them in *N*-methyl-2-pyrrolidinone (NMP). Before the injection of NMP, the ground mixture was sufficiently dried overnight in vacuum at 80 °C. The weight of the ground mixture was measured before and after vacuum drying to ensure that water was eliminated as much as possible. The working electrode with a mass loading of ∼3 mg cm^{-2} was prepared by spreading the slurry on a graphite paper current collector (Alfa Aesar) followed by drying overnight in vacuum at 60 °C.

4.4. Electrochemical Characterization. To perform the electrochemical measurements, we prepared a two-electrode half-cell containing the working electrode and sufficient lithium metal (reference electrode) in an argon-filled glove box. $LiPF_6$ was flooded into a 1:1 (v/v) mixture of ethylene carbonate and diethylene carbonate.

The EIS of the electrode was measured with an Im6ex ZAHNER impedance measuring instrument in a half-cell with the frequency range being 10 mHz to 1 MHz under a voltage amplitude of 10 mV.

Galvanostatic charge/discharge measurements were performed between 2.2 and 4.5 V versus Li^+/Li at current densities of 0.1, 0.2, 0.4, 0.6, 0.8, and 1 A g^{-1}. The long-term galvanostatic charge/discharge cycling tests of FeHCCo and CeHCCo were conducted at 0.1 A g^{-1} up to 100 cycles. All of the current densities and specific capacities reported in this work were calculated based on the weight of the active material (FeHCCo or CeHCCo).

■ ASSOCIATED CONTENT

Supporting Information

The Supporting Information is available free of charge at https://pubs.acs.org/doi/10.1021/acsomega.9b03104.

HRTEM, SEM, and EDS images of the FeHCCo and CeHCCo NPs; EDX mapping of the FeHCCo and CeHCCo; XRF mapping for the as-prepared FeHCCo and CeHCCo; XPS for the as-prepared FeHCCo and CeHCCo; XPS spectra for FeHCCo and CeHCCo; representative charge/discharge curves for FeHCCo and CeHCCo; charge/discharge cycling measurement and representative charge/discharge curves of graphite paper current collector; schematic illustration of the discharge process of FeHCCo and CeHCCo; EIS spectra of FeHCCo and CeHCCo; the corresponding equivalent circuit; XRD spectra of FeHCCo and CeHCCo before and after charge/discharge cycling measurements; quantitative elemental characterization for the as-prepared FeHCCo and CeHCCo; quantitative elemental characterization for the as-prepared FeHCCo and CeHCCo by ICP; and a comparison in capacity of the CeHCCo product and other reported Prussian blue analogues (PDF)

■ AUTHOR INFORMATION

Corresponding Authors

*E-mail: varma.rajender@epa.gov (R.S.V.).
*E-mail: jwchoi@kist.re.kr (J.-W.C.).
*E-mail: hwjang@snu.ac.kr (H.W.J.).
*E-mail: mrsh2@snu.ac.kr (M.S.).

ORCID

Kaiqiang Zhang: 0000-0002-2288-4893
Rajender S. Varma: 0000-0001-9731-6228
Ji-Won Choi: 0000-0002-7701-3227
Ho Won Jang: 0000-0002-6952-7359
Mohammadreza Shokouhimehr: 0000-0003-1416-6805

Notes

The authors declare no competing financial interest.

■ ACKNOWLEDGMENTS

This research was supported by the Korea Institute of Science and Technology Future Resource Program (no. 2E29400). Furthermore, the financial support from the Future Material Discovery Program (no. 2016M3D1A1027666), Basic Science Research Program (no. 2017R1A2B3009135) through the National Research Foundation of Korea, and China Scholarship Council (no. 201808260042) is appreciated.

■ REFERENCES

(1) Ma, L.; Chen, T.; Zhu, G.; Hu, Y.; Lu, H.; Chen, R.; Liang, J.; Tie, Z.; Jin, Z.; Liu, J. Pitaya-like microspheres derived from Prussian blue analogues as ultralong-life anodes for lithium storage. *J. Mater. Chem. A* **2016**, *4*, 15041−15048.

(2) Ma, L.; Chen, R.; Zhu, G.; Hu, Y.; Wang, Y.; Chen, T.; Liu, J.; Jin, Z. Cerium oxide nanocrystal embedded bimodal micro-mesoporous nitrogen-rich carbon nanospheres as effective sulfur host for lithium-sulfur batteries. *ACS Nano* **2017**, *11*, 7274−7283.

(3) Ma, L.; Chen, R.; Hu, Y.; Zhu, G.; Chen, T.; Lu, H.; Liang, J.; Tie, Z.; Jin, Z.; Liu, J. Hierarchical porous nitrogen-rich carbon nanospheres with high and durable capabilities for lithium and sodium storage. *Nanoscale* **2016**, *8*, 17911−17918.

(4) Chen, T.; Cheng, B.; Chen, R.; Hu, Y.; Lv, H.; Zhu, G.; Wang, Y.; Ma, L.; Liang, J.; Tie, Z.; Jin, Z.; Liu, J. Hierarchical ternary carbide nanoparticle/carbon nanotube-inserted N-doped carbon concave-polyhedrons for efficient lithium and sodium storage. *ACS Appl. Mater. Interfaces* **2016**, *8*, 26834−26841.

(5) Deng, J.; Luo, W.-B.; Lu, X.; Yao, Q.; Wang, Z.; Liu, H.-K.; Zhou, H.; Dou, S.-X. High Energy Density Sodium-Ion Battery with

DOI: 10.1021/acsomega.9b03104
ACS Omega 2019, 4, 21410−21416

Industrially Feasible and Air-Stable O3-Type Layered Oxide Cathode. *Adv. Energy Mater.* **2018**, *8*, 1701610.
(6) Wang, T.; Yang, H.; Lu, B. Ultra-stable sodium ion battery cathode realized by Cu_7S_4 nanoparticles. *J. Power Sources* **2018**, *399*, 105−114.
(7) Yang, D.; Xu, J.; Liao, X. Z.; He, Y.-S.; Liu, H.; Ma, Z.-F. Structure optimization of Prussian blue analogue cathode materials for advanced sodium ion batteries. *Chem. Commun.* **2014**, *50*, 13377−13380.
(8) Lee, H.; Kim, Y.-I.; Park, J.-K.; Choi, J. W. Sodium zinc hexacyanoferrate with a well-defined open framework as a positive electrode for sodium ion batteries. *Chem. Commun.* **2012**, *48*, 8416−8418.
(9) Zhang, C.; Xu, Y.; Zhou, M.; Liang, L.; Dong, H.; Wu, M.; Yang, Y.; Lei, Y. Potassium Prussian blue nanoparticles: a low-cost cathode material for potassium-ion batteries. *Adv. Funct. Mater.* **2017**, *27*, 1604307.
(10) Deng, L.; Yang, Z.; Tan, L.; Zeng, L.; Zhu, Y.; Guo, L. Investigation of the Prussian blue analog $Co_3[Co(CN)_6]_2$ as an anode material for nonaqueous potassium-ion batteries. *Adv. Mater.* **2018**, *30*, 1802510.
(11) Wessells, C. D.; Peddada, S. V.; Huggins, R. A.; Cui, Y. Nickel hexacyanoferrate nanoparticle electrodes for aqueous sodium and potassium ion batteries. *Nano Lett.* **2011**, *11*, 5421−5425.
(12) Jiang, X.; Zhang, T.; Yang, L.; Li, G.; Lee, J. Y. A Fe/Mn-based Prussian blue analogue as a K-rich cathode material for potassium-ion batteries. *ChemElectroChem* **2017**, *4*, 2237−2242.
(13) Xia, C.; Guo, J.; Lei, Y.; Liang, H.; Zhao, C.; Alshareef, H. N. Rechargeable aqueous zinc-ion battery based on porous framework zinc pyrovanadate intercalation cathode. *Adv. Mater.* **2018**, *30*, 1705580.
(14) Kundu, D.; Vajargah, S. H.; Wan, L.; Adams, B.; Prendergast, D.; Nazar, L. F. Aqueous vs. nonaqueous Zn-ion batteries: consequences of the desolvation penalty at the interface. *Energy Environ. Sci.* **2018**, *11*, 881−892.
(15) Zhang, K.; Lee, T. H.; Bubach, B.; Ostadhassan, M.; Jang, H. W.; Choi, J.-W.; Shokouhimehr, M. Coordinating gallium hexacyanocobaltate: Prussian blue-based nanomaterial for Li-ion storage. *RSC Adv.* **2019**, *9*, 26668−26675.
(16) Zhang, K.; Lee, T. H.; Noh, H.; Islamoglu, T.; Farha, O. K.; Jang, H. W.; Choi, J.-W.; Shokouhimehr, M. Realization of lithium-ion capacitors with enhanced energy density via the use of gadolinium hexacyanocobaltate as a cathode material. *ACS Appl. Mater. Interfaces* **2019**, *11*, 31799−31805.
(17) Zhang, K.; Lee, T. H.; Jang, H. W.; Shokouhimehr, M.; Choi, J.-W. A hybrid energy storage mechanism of zinc hexacyanocobaltate-based metal-organic framework endowing stationary and high-performance lithium-ion storage. *Electron. Mater. Lett.* **2019**, *15*, 444−453.
(18) Zhang, K.; Varma, R. S.; Jang, H. W.; Choi, J.-W.; Shokouhimehr, M. Iron hexacyanocobaltate metal-organic framework: highly reversible and stationary electrode material with rich borders for lithium-ion batteries. *J. Alloys Compd.* **2019**, *791*, 911−917.
(19) Jiang, Y.; Takahashi, A.; Kawamoto, T.; Asai, M.; Zhang, N.; Lei, Z.; Zhang, Z.; Kojima, K.; Imoto, K.; Nakagawa, K.; Ohkoshi, S.; Nakamura, T. High performance sorption and desorption behaviours at high working temperatures of ammonia gas in a cobalt-substituted Prussian blue analogue. *Chem. Commun.* **2018**, *54*, 11961−11964.
(20) Hartman, M. R.; Peterson, V. K.; Liu, Y.; Kaye, S. S.; Long, J. R. Neutron diffraction and neutron vibrational spectroscopy studies of hydrogen adsorption in the Prussian blue analogue $Cu_3[Co(CN)_6]_2$. *Chem. Mater.* **2006**, *18*, 3221−3224.
(21) Shokouhimehr, M. Prussian blue nanoparticles and its analogues as new-generation T1-weighted MRI contrast agents for cellular imaging. Kent State University, 2010.
(22) Huang, S. D.; Li, Y.; Shokouhimehr, M. Gadolinium containing Prussian blue nanoparticles as nontoxic MRI contrast agents having high relaxivity. U.S. Patent 20,100,254,912, 2010.
(23) Huang, S. D.; Basu, S.; Khitrin, A. K.; Shokouhimehr, M.; Soehnlen, E. S. Materials and methods for MRI contrast agents and drug delivery. U.S. Patent 8,580,230, 2013.
(24) Gerbaldi, C.; Nair, J. R.; Kulandainathan, M. A.; Kumar, R. S.; Ferrara, C.; Mustarelli, P.; Stephan, A. M. Innovative high performing metal organic framework (MOF)-laden nanocomposite polymer electrolytes for all-solid-state lithium batteries. *J. Mater. Chem. A* **2014**, *2*, 9948−9954.
(25) Aubrey, M. L.; Ameloot, R.; Wiers, B. M.; Long, J. R. Metal-organic frameworks as solid magnesium electrolytes. *Energy Environ. Sci.* **2014**, *7*, 667−671.
(26) Jia, S.; Zang, J.; Li, W.; Tian, P.; Zhou, S.; Cai, H.; Tian, X.; Wang, Y. A novel synthesis of Prussian blue nanocubes/biomass-derived nitrogen-doped porous carbon composite as a high-efficiency oxygen reduction reaction catalyst. *Electrochim. Acta* **2018**, *289*, 56−64.
(27) Li, X.; Liu, J.; Rykov, A. I.; Han, H.; Jin, C.; Liu, X.; Wang, J. Excellent photo-fenton catalysts of Fe-Co Prussian blue analogues and their reaction mechanism study. *Appl. Catal., B* **2015**, *179*, 196−205.
(28) Yu, S.-H.; Guo, X.; Ling, D.; Chung, D. Y.; Jin, A.; Shokouhimehr, M.; Hyeon, T.; Sung, Y.-E. Facile synthesis of nanostructured carbon nanotube/iron oxide hybrids for lithium-ion battery anodes. *RSC Adv.* **2014**, *4*, 37365−37370.
(29) Zhang, K.; Lee, T. H.; Bubach, B.; Ostadhassan, M.; Jang, H. W.; Choi, J.-W.; Shokouhimehr, M. Layered metal-organic framework based on tetracycanonickelate as a cathode material for in situ Li-ion storage. *RSC Adv.* **2019**, *9*, 21363−21370.
(30) Buser, H. J.; Schwarzenbach, D.; Petter, W.; Ludi, A. The crystal structure of Prussian blue: $Fe_4[Fe(CN)_6]_3{\cdot}xH_2O$. *Inorg. Chem.* **1977**, *16*, 2704−2710.
(31) Matsuda, T.; Moritomo, Y. Thin film electrode of Prussian blue analogue for Li-ion battery. *Appl. Phys. Express* **2011**, *4*, No. 047101.
(32) Paolella, A.; Faure, C.; Timoshevskii, V.; Marras, S.; Bertoni, G.; Guerfi, A.; Vijh, A.; Armand, M.; Zaghib, K. A review on hexacyanoferrate-based materials for energy storage and smart windows: challenges and perspectives. *J. Mater. Chem. A* **2017**, *5*, 18919−18932.
(33) Wang, H.; Zhu, Q.; Li, H.; Xie, C.; Zeng, D. Tuning the particle size of Prussian blue by a dual anion source method. *Cryst. Growth Des.* **2018**, *18*, 5780−5789.
(34) Adak, S.; Daemen, L. L.; Hartl, M.; Williams, D.; Summerhill, J.; Nakotte, H. Thermal expansion in 3D-metal Prussian blue analogs-a survey study. *J. Solid State Chem.* **2011**, *184*, 2854−2861.
(35) Shokouhimehr, M.; Yu, S.-H.; Lee, D.-C.; Ling, D.; Hyeon, T.; Sung, Y.-E. Metal hexacyanoferrate nanoparticles as electrode materials for lithium ion batteries. *Nanosci. Nanotechnol. Lett.* **2013**, *5*, 770−774.
(36) Yang, D.; Xu, J.; Liao, X.-Z.; Wang, H.; He, Y.-S.; Ma, Z.-F. Prussian blue without coordinated water as a superior cathode for sodium-ion batteries. *Chem. Commun.* **2015**, *51*, 8181−8184.
(37) Nie, P.; Shen, L.; Luo, H.; Ding, B.; Xu, G.; Wang, J.; Zhang, X. Prussian blue analogues: a new class of anode materials for lithium ion batteries. *J. Mater. Chem. A* **2014**, *2*, 5852−5857.
(38) Zgârian, R. G.; Tihan, G. T.; Kajzar, F.; Rău, I.; Pawlicka, A.; Mîndroiu, M. V. Chromophore doped DNA based solid polymer electrolyte for electrochromic devices. *Arab. J. Chem.* **2017**, *10*, 232−239.
(39) You, Y.; Yu, X.; Yin, Y.; Nam, K.-W.; Guo, Y.-G. Sodium iron hexacyanoferrate with high Na content as a Na-rich cathode material for Na-ion batteries. *Nano Res.* **2015**, *8*, 117−128.
(40) Barsan, M. M.; Butler, I. S.; Fitzpatrick, J.; Gilson, D. F. R. High-pressure studies of the micro-Raman spectra of iron cyanide complexes: Prussian blue ($Fe_4[Fe(CN)_6]_3$), potassium ferricyanide ($K_3[Fe(CN)_6]$), and sodium nitroprusside ($Na_2[Fe(CN)_5(NO)]{\cdot}2H_2O$). *J. Raman Spectrosc.* **2011**, *42*, 1820−1824.
(41) Okubo, M.; Honma, I. Ternary metal Prussian blue analogue nanoparticles as cathode materials for Li-ion batteries. *Dalton Trans.* **2013**, *42*, 15881−15884.

DOI: 10.1021/acsomega.9b03104
ACS Omega 2019, 4, 21410−21416

(42) Rogers, D. M.; Johansson, J. O. Metal-to-metal charge-transfer transitions in Prussian blue hexacyanochromate analogues. *Mater. Sci. Eng., B* **2018**, *227*, 28−38.
(43) Koumousi, E. S.; Jeon, I.-R.; Gao, Q.; Dechambenoit, P.; Woodruff, D. N.; Merzeau, P.; Buisson, L.; Jia, X.; Li, D.; Volatron, F.; Mathonière, C.; Clérac, R. Metal-to-metal electron transfer in Co/Fe Prussian blue molecular analogues: the ultimate miniaturization. *J. Am. Chem. Soc.* **2014**, *136*, 15461−15464.
(44) Sindoro, M.; Yanai, N.; Jee, A.-Y.; Granick, S. Colloidal-sized metal-organic frameworks: synthesis and applications. *Acc. Chem. Res.* **2013**, *47*, 459−469.
(45) Zhou, H.-C.; Kitagawa, S. Metal-organic frameworks (MOFs). *Chem. Soc. Rev.* **2014**, *43*, 5415−5418.
(46) Zakaria, M. B.; Chikyow, T. Recent advances in Prussian blue and Prussian blue analogues: synthesis and thermal treatments. *Coord. Chem. Rev.* **2017**, *352*, 328−345.
(47) Ming, H.; Torad, N. L. K.; Chiang, Y.-D.; Wu, K. C.-W.; Yamauchi, Y. Size- and shape-controlled synthesis of Prussian blue nanoparticles by a polyvinylpyrrolidone-assisted crystallization process. *Cryst. Eng. Commun.* **2012**, *14*, 3387−3396.
(48) Ikeda, K.; Schneider, H.; Akasaka, M.; Rager, H. Crystal-field spectroscopic study of Cr-doped mullite. *Am. Mineral.* **1992**, *77*, 251−257.
(49) Nai, J.; Guan, B. Y.; Yu, L.; Lou, X. W. Oriented assembly of anisotropic nanoparticles into frame-like superstructures. *Sci. Adv.* **2017**, *3*, No. e1700732.
(50) Lin, M.; Tng, L.; Lim, T.; Choo, M.; Zhang, J.; Tan, H. R.; Bai, S. Hydrothermal synthesis of octadecahedral hematite (α-Fe_2O_3) nanoparticles: an epitaxial growth from goethite (α-FeOOH). *J. Phys. Chem. C* **2014**, *118*, 10903−10910.
(51) Zheng, G.; Lee, S. W.; Liang, Z.; Lee, H.-W.; Yan, K.; Yao, H.; Wang, H.; Li, W.; Chu, S.; Cui, Y. Interconnected hollow carbon nanospheres for stable lithium metal anodes. *Nat. Nanotechnol.* **2014**, *9*, 618−623.
(52) Li, Q.; Zhu, S.; Lu, Y. 3D porous Cu current collector/Li-metal composite anode for stable lithium-metal batteries. *Adv. Funct. Mater.* **2017**, *27*, 1606422.
(53) Zhao, B.; Zhang, G.; Song, J.; Jiang, Y.; Zhuang, H.; Liu, P.; Fang, T. Bivalent tin ion assisted reduction for preparing graphene/SnO_2 composite with good cyclic performance and lithium storage capacity. *Electrochim. Acta* **2011**, *56*, 7340−7346.
(54) Mazinani, B.; Kazazi, M.; Mobarhan, G.; Shokouhimehr, M. The combustion synthesis of Ag-doped $MnCo_2O_4$ nanoparticles for supercapacitor applications. *JOM* **2019**, *71*, 1499−1506.
(55) Yu, S.-H.; Shokouhimehr, M.; Hyeon, T.; Sung, Y. E. Iron hexacyanoferrate nanoparticles as cathode materials for lithium and sodium rechargeable batteries. *ECS Electrochem. Lett.* **2013**, *2*, A39−A41.
(56) Shokouhimehr, M.; Soehnlen, E. S.; Hao, J.; Griswold, M.; Flask, C.; Fan, X.; Basilion, J. P.; Basu, S.; Huang, S. D. Dual purpose Prussian blue nanoparticles for cellular imaging and drug delivery: a new generation of T1-weighted MRI contrast and small molecule delivery agents. *J. Mater. Chem.* **2010**, *20*, 5251−5259.
(57) Shokouhimehr, M.; Soehnlen, E. S.; Khitrin, A.; Basu, S.; Huang, S. D. Biocompatible Prussian blue nanoparticles: preparation, stability, cytotoxicity, and potential use as an MRI contrast agent. *Inorg. Chem. Commun.* **2010**, *13*, 58−61.
(58) Bie, X.; Kubota, K.; Hosaka, T.; Chihara, K.; Komaba, S. Synthesis and electrochemical properties of Na-rich Prussian blue analogues containing Mn, Fe, Co, and Fe for Na-ion batteries. *J. Power Sources* **2018**, *378*, 322−330.
(59) Sun, D.; Wang, H.; Deng, B.; Zhang, H.; Wang, L.; Wan, Q.; Yan, X.; Qu, M. A Mn-Fe based Prussian blue Analogue@Reduced graphene oxide composite as high capacity and superior rate capability anode for lithium-ion batteries. *Carbon* **2019**, *143*, 706−713.

DOI: 10.1021/acsomega.9b03104
ACS Omega 2019, 4, 21410−21416